Article:

Craig, TJ and Heyburn, R (2015) An enigmatic earthquake in the continental mantle lithosphere of stable North America. Earth and Planetary Science Letters, 425. 12 - 23. ISSN 1385-013X

https://doi.org/10.1016/j.epsl.2015.05.048

An enigmatic earthquake in the continental mantle lithosphere of stable North America

As accepted for publication

T. J. Craig[1], R. Heyburn[2]

[1] Laboratoire de Geologie, Ecole Normale Supérieure, 24 rue Lhomond, Paris, France.

[2] AWE Blacknest, Brimpton, Reading, RG7 4RS, United Kingdom.

Corresponding author email: craig@geologie.ens.fr

November 23, 2015

Abstract

The existence of earthquakes within continental lithospheric mantle remains a highly controversial topic. Here, we present a detailed set of seismological analyses confirming the occurrence of a mantle earthquake beneath the Wind River Range of central Wyoming. Combining regional waveform inversion with the analysis of the delay and relative amplitudes of teleseismically-observed depth phases, we demonstrate that the 2013 Wind River earthquake – a M_W 4.7 highly-oblique thrust-faulting event – occurred at 75 ± 8km, well beneath the base of the crust. The magnitude, mechanism, and location of this earthquake suggest that it represents simple brittle failure at relatively high temperatures within the mantle lithosphere, as a result of tectonic, rather than magmatic, processes.

Keywords: Continental lithosphere, rheology, earthquake seismology, mantle earthquake.

Highlights:

- Detailed source analysis of a M_W 4.7 earthquake in central Wyoming
- A rare example of an earthquake occurring in continental lithospheric mantle
- Source depth of 75 ± 8 km places it conclusively below the Moho
- Waveform similarity suggests the only aftershock occurred at a similar depth

1 Introduction

The occurrence and significance of earthquakes in the mantle lithosphere of stable continental regions has been a subject of much debate (e.g. Chen and Molnar, 1983; Wong and Chapman, 1990; Zhu and Helmberger, 1996; Maggi et al., 2000; Chen and Yang, 2004; Priestley et al., 2008; Sloan and Jackson, 2012), with their existence and location being used to argue for different rheological models for the continental lithosphere (e.g. Chen and Molnar, 1983; Jackson et al., 2008; Burov, 2010). Whilst earthquakes in the mantle of oceanic lithosphere are commonplace (e.g. Wiens and Stein, 1983; Craig et al., 2014), well-constrained examples from continental lithosphere are comparatively rare. Confirmed earthquakes in the continental mantle are limited to Utah (Zandt and Richins, 1979), northern Australia (Sloan and Jackson, 2012), and potentially northern India and Tibet (Chen and Molnar, 1983; Zhu and Helmberger, 1996; Chen and Yang, 2004; Priestley et al., 2008; Craig et al., 2012), although the precise location of deep earthquakes with respect to the local Moho in this latter case remains uncertain. Occasional other earthquakes at mantle depths in continental areas are reported in routine earthquake catalogues (e.g. International Seismological Centre, 2012; Engdahl et al., 1998). However, given the degree of precision required to differentiate earthquakes in the crust and uppermost mantle, and the uncertainties in such techniques, these often prove to be false or unverifyable when subjected to more detailed analyses aimed specifically at depth determination (Maggi et al., 2000; Engdahl et al., 2006). How widespread mantle seismicity in continental regions may be, and the depth extent over which it can occur, therefore remains a topic severely limited by a paucity of high-quality observational constraints.

As a result of the well-established thermal control on brittle failure of the lithosphere, potential mantle earthquakes in stable continental regions are expected to concentrate in the uppermost (and therefore coldest) few kms of the mantle, close to the Moho. The confirmation of an earthquake as occurring in mantle lithosphere, rather than in the overlying lower crust, thus typically requires precise knowledge of both the depth of the earthquake, and the depth of the Moho in the source region. Uncertainties in both parameters often result in earthquake depths within error of the local Moho, which cannot be conclusively identified as either crustal or mantle in origin.

Here, we present a comprehensive seismological study of an earthquake located near the Wind River range in central Wyoming, identified by the NEIC Preliminary Determination of Epicenters bulletin (NEIC hereafter) as having a potentially mantle origin. The location of this earthquake, within the continental United States, and the large amount of high-quality seismic data available make it ideal for a detailed analysis to confirm the preliminary NEIC depth. We combine regional seismological estimates of the earthquake focal mechanism and depth with teleseismic depth phase observations from both individual broadband stations and from small-to-medium aperture multi-instrument arrays to present conclusive evidence in favour of a hypocentre located significantly below the base of the crust in this region, well into the lithospheric mantle. We then briefly discuss the regional context of this earthquake, and how it may impact on current models for the rheology of continental lithosphere.

2 The 2013 Wind River Earthquake

This paper focuses on an earthquake that occurred in central Wyoming, between the Wind River Range and Wind River Basin (Figure 1). The Wind River region is relatively seismically quiescent, with instrumentally recorded seismicity, covering a period of ~ 60 years, rarely exceeding M_L

4, and only once having reached M_L 5. The region lies within the central Wyoming Craton, near the complex western boundary of the cold, stable lithosphere which underlies much of northern North America, west of the Rocky Mountains (e.g. Sigloch, 2011; Porritt et al., 2014). The present day topography largely reflects deformation during the Late Cretaceous/Jurassic Laramide orogeny, of which the Wind River mountains represent a distal part. The Range itself is a basement-cored uplift, bounded by major (but inactive) crustal faults on its southwestern side, within the Archean Wyoming craton. The centre of the range comprises crystalline rocks of Archean age. The Wind River basin contains Paleozoic sediments, overlying the Archean basement. At present, the region is tectonically inactive, with the nearest region of significant seismicity being that related to the Yellowstone Hotspot (and associated track), some 200 km to the northwest.

At 13:16:33 UTC on the 21^{st} September 2013, a moderate magnitude earthquake ($M_W \sim 4.8$) was reported in the area of the Wind River Range, Wyoming (42.974°N, 109.128°W; NEIC). Initial estimates of the earthquake depth, based on routine travel time inversion (NEIC) and surface and very-long-period body-wave inversion (`www.globalcmt.org`) indicated that this earthquake originated in the mantle lithosphere, at between 70 and 80 km. Hypocentral locations from both catalogues indicate a source beneath the margin between the mountains and the adjacent basin. Here, we undertake a detailed investigation aimed at confirming a source location in the mantle lithosphere for this earthquake.

A single aftershock was reported by the NEIC, occurring two hours after the initial earthquake. The reported catalogue depth of this event is similar (71 km) to that reported for the mainshock (76 km). Whilst the magnitude of this earthquake (M_L 3.0) makes it too small to be analysed with the methods employed here to study the mainshock, we use similarity in S-P arrival times and in apparent vector slowness across a regional array, to suggest that its depth is similar to that of the mainshock.

3 Earthquake source parameters

3.1 Velocity model

The seismological analyses conducted in this study are all heavily dependent on the near-source velocity structure. In the case of the regional inversion, a layered 1-dimensional model is used to calculate Greens functions for the computation of synthetic seismograms. For stations at greater distances, the same model is used to calculate depth-phase delay times and synthetic waveforms. The use of a simple one-dimensional velocity model fails to account for lateral variations in the velocity structure around the source. However, the precise details of the local velocity structure are largely unknown, and cannot be included accurately. The velocity model used (Table S1) is based on the "Western US" model used by Herrmann et al. (2011), who modified an earlier model developed by the University of Utah in the Yellowstone area, in order to fit regional surface-wave dispersion measurements across Wyoming and Utah. Our principle modifications to this model arise from accounting for the local Moho depth, particularly relevant for the accurate conversion of depth-phase delay times to a source depth, and minor changes to the nearest-surface layer to match teleseismic sP-phase amplitudes.

Moho depth in the region is known to vary on a local scale between $\sim$ 40 km under the Wind River Range, to $\sim$ 50 km under the adjacent basin, based on a the results of the Deep Probe seismic transect (Snelson et al., 1998). This range of crustal thickness estimates is comparable to those determined through a combination of surface wave dispersion measurements and teleseismic receiver functions (42–50 km; Shen et al., 2013). In our preferred model, we take an intermediate crustal thickness value of 45 km (Table S1).

We further alter the velocities in the near-surface layer slightly from the original model of Herrmann et al. (2011), to improve the amplitude fit of the synthetic seismograms calculated in Section 3.7, in particular the amplitudes of the sP phase.

3.2 Regional waveform inversion

To determine a source mechanism, and for an initial estimate of the source depth, we employ a time-domain regional waveform inversion routine (based on that of Herrmann, 2013). We select available data from broadband and high-gain seismometers within 600 km of the NEIC earthquake epicentre. Seismograms, with the station response removed, are subjected to a four-pole Butterworth filter, with a pass band in the range 0.02–0.08 Hz. This frequency range has the advantage of removing sensitivity to short-wavelength variations in the velocity structure which, as stated earlier, are not included in our regional velocity model.

Greens functions are calculated by wavenumber integration for the velocity model described above for event-station distances based on the separation between available stations and the NEIC earthquake location (see Figure 1(b)). Synthetic seismograms are then created for each station based on the Greens functions for the epicentral distance, assuming a simple pulse source, and filtered for the same frequency range used for the observed data. We also assume that the source mechanism can be appropriately represented by a double-couple, and calculate the relative amplitudes of the synthetic seismograms appropriately.

Alignment between observed and synthetic waveforms is based on the first P-wave arrival, calculated for the synthetic waveform, and manually picked on the observed waveform prior to filtering. To account for potential errors in the onset determination, a timeshift of up to 0.5 seconds is allowed during inversion, with the optimum shift being determined by maximising a cross correlation function between the synthetic and observed seismograms over the ± 0.5 s window around the picked arrival.

The fit in for each set of synthetic seismograms is determined using the function (f_r) such that

$$f_r(\theta, \delta, \phi, z) = 1 - \frac{(\sum_i^N \sum_j u_{ij} s_{ij})^2}{(\sum_i^N \sum_j u_{ij}^2)(\sum_i^N \sum_j s_{ij}^2)} \tag{1}$$

where u_{ij} and s_{ij} are the jth sample of ith observed and synthetic waveforms respectively, for a total of a total of N observed waveforms, and θ,δ,ϕ,z are the strike, dip, rake, and source depth.

A best-fit solution is determined for each depth increment through a grid search over a parameter range encompassing the full range of possible mechanism parameters in 5° increments for strike, dip and rake. Seismic moment is calculated based on the best-fit amplitude scaling for the synthetic seismograms. Best-fit mechanisms are determined for the depth range 1 – 150 km, in 1 km increments. Figure 2 shows the results of this inversion.

A clear minimum is seen in the misfit with depth at 78 km, with the source parameters $\theta = 060°$, $\delta = 60°$, $\phi = 025°$, $M_W = 4.72$. The source mechanism is in good agreement with that determined by the gCMT project (www.globalcmt.org), and is largely independent of the source depth. Using a similar method, Frolich et al. (2015) reported a best-fit regional source depth of 72–76 km, depending on the precise details of the velocity model used, again in good agreement with our results.

Given the uncertainties present in the velocity model, particularly for the depth of the Moho, we perform similar inversions for a range of velocity models with Moho depths ranging from 40 – 50 km (based on increasing the thickness of the lowest crustal layer in Table S1). Minimum misfit source depths for this range vary from 75 to 84 km, and are all contained within a relatively broad but well-defined minima in the misfit function. In all cases, the minimum misfit source depths are $>$ 25 km below the Moho, and there is minimal variation in the best-fit source mechanism.

Similarly, we undertake a series of separate inversions based on the different catalogue epicenters available, with a maximum horizontal separation of 50 km. Locations within $\sim$ 25 km of the NEIC epicenter result in only minor variations in the minimum misfit, little change in mechanism, and a variation in best-fit depth of $\leq$ 3 km. At greater variations in epicenter, misfit begins to increase sharply, verifying the applicability of the NEIC epicenter to within $\sim$25 km. This relative insensitivity to small changes in epicentral location is likely due to a combination of the removal of absolute travel times from the inversion, the uneven distribution of stations around the focal sphere, and the lack of stations close ($\lesssim$140 km) to the source, due to saturation of the few seismometers at closer distances.

To assist in the investigation of potential source processes behind this earthquake, we test how appropriate the assumption of a double-couple source is by also inverting at each depth for a best-fit unconstrained moment tensor, allowing the incorporation of volumetric and deviatoric components into the source mechanism. Whilst this does lead to a slight improvement in the fit to the data, the percentage non-double-couple component remains low in all cases ($< 15\%$), and the orientation of the double-couple component being similar to that from the inversion for a pure double-couple source, and the best-fit depth differs by 1 km from the pure double-couple case. As a result, we conclude that the marginal decrease in misfit does not warrant the inclusion of a non-double-couple component.

3.3 Depth phase analyses

Whilst short-range regional waveform inversion allows us to place initial constraints on the earthquake depth, the misfit minimum remains broad, with a wide range of possible depths capable of fitting the observed waveforms well. Figures S1 and S2 show waveform misfits for the best-fit mechanisms at ± 10 and ± 20 km relative to the minimum misfit depth. As these figures demonstrate, variations of ≤ 10 km in depth produce little change in misfit to the minimum, and it is only at larger variations that significant differences between regional waveforms emerge. Whilst this strongly indicates a sub-crustal source, a significant increase in the precision of the estimated source depth can be derived from the delay times of depth phases (near-source surface reflections), relative to the direct arrival, in seismograms recorded at teleseismic distances from the earthquake source. The use of data at large epicentral distances allows the path followed by the direct arrival and depth phases following their reflection to be taken as approximately the same. Depths derived from this methodology are independent of the absolute travel time and the velocity structure along the majority of the raypath, and depend only on the above-source velocity structure.

We select broadband seismograms at epicentral distances appropriate for the observation of depth phases (20 – 90°) from regions where such phases are expected to be of high amplitude, and hence observable, based on the radiation pattern for the focal mechanism derived from the regional inversion. We split these observations into two categories – those stations at 30 – 90°, where depth phases delay times are expected to be unique for each phase, and those stations at 20 – 30°, where depth phases, whilst still present and interpretable, may not be unique in their arrival times due to potential triplications, depending on the precise nature of the whole-Earth velocity structure.

Figures 3 and S3 show selected seismograms where depth-phase arrivals are visible for the 20 – 30° distance range. On all the stations shown, a clear arrival can be identified within 1s of the predicted pP arrival time for a depth of 75 km. Whilst in some cases this arrival is a short isolated pulse (e.g., TKL, D52A), in many cases, it is followed by a complex series of arrivals over the following ∼5s, consistent with predicted triplicate arrivals. On a number of stations, a subsequent arrival coincident with the predicted sP time can be identified (e.g., ODNJ, NCB, G54A, T53A).

Figure 4 shows teleseismic waveforms where depth-phases can be observed without the complication of phase triplications. Whilst, due to attenuation, the signals become increasingly less clear with distance from the source, arrivals consistent with the pP arrival time (±2s) can be seen at a number of stations (e.g., ABKAR, SMRT, SIV, LPAZ). Similarly, arrivals at the approximate time predicted for the sP phase can also be seen, although more rarely (e.g, LVZ, CCB, MLY, COLA).

On several stations shown on Figures 3 and 4, low-amplitude arrivals can be identified at ∼ 8s after the direct P-wave arrival (e.g., G54A, M54A, LPAZ, CCB, MLY). Whilst interpreting such low amplitude phases is complex, we note that these are at the expected time for depth-phase reflections from the Moho, given the uncertainty in the depth of this interface.

3.4 Waveform analysis from array data

To enhance the signal-to-noise ratio, we also make use of available small-to-medium aperture array data at teleseismic distances (one in Europe, three in Asia, and one in North America). The locations of these arrays are shown on Figure 4 by the blue circles. The results of the analysis of these arrays are shown on Figure 5.

In each case, data from across the array are beamformed using the expected backazimuth and slowness for the direct P arrival. To aid in identifying coherent signals across the array, we employ the F-statistic tests described in Heyburn and Bowers (2008). Following Blandford (1974), the F-statistic is defined as the power of the beam divided by the average difference between each individual trace in the array (after time-shifting) and the beam, time-averaged over a boxcar window, such that:

$$F(t) = (N-1)\frac{\sum_{t=1}^{M} \hat{u}(t)^2}{\left(\frac{1}{N}\sum_{i=1}^{N}\sum_{t=1}^{M} u_i(t)^2 - \sum_{t=1}^{M} \hat{u}(t)^2\right)} \quad (2)$$

where N denotes the number of traces used, $u_i(t)$ denotes the amplitude from instrument i at time t, $\hat{u}(t)$ the beam, and M represents averaging over a boxcar window of width M seconds. The arrival of coherent signals at the slowness and azimuth used in constructing the beam results in large values of F, whereas when only random, uncorrelated noise is present, F is expected to tend to 1.

For each array, we also construct vespagrams, assessing the incoming signal coherence (via the F-statistic) as a function of time and ray parameter, to confirm that the signals being received are originating from the correct geographic region (Figure 5). Spatial resolution for the signal source is relatively poor, due to the small aperture width of the arrays used, particularly for the smaller arrays at MKAR, PETK and USRK (apertures of $\sim$4 km). However, similarities between the apparent slowness of the direct arrival and of later arriving signals serves to confirm that the interpreted signal is not background noise, and is not a coherent signal from another spatially-separated source.

A clear pP arrival can be seen in both the beam and the F-trace at ESDC, and this is then followed by a low amplitude, high coherence signal consistent with sP. The sP phase is particularly clear in both the beam and F-trace at ILAR and USRK. MKAR and PETK also show evidence for low-amplitude, high-coherence arrivals, although in both cases they are slightly later than predicted. All arrays show the arrival of low amplitude signals, low coherence arrivals at other points in the waveform, both before and after the much larger amplitude depth phase arrivals. Whilst the vespagrams demonstrate that these are indeed coherent signals originating from the approximate source region, given their similar apparent slownesses to the direct arrival, due to their low amplitude, we interpret these as Moho/intracrustal reflections and conversions, arising from impedance contrasts in either the near-source or near receiver velocity structure.

In both the single-station data shown in Figure 4 and in the array data on Figure 5 a single depth value is unable to precisely match the observed depth phase delay times at all stations, with discrepancies for our best-fit depth (75 km, based on the optimum fit to predicted arrival times) ranging up to 2 seconds. This likely represents the three-dimensional nature of the near-source velocity structure, which is not well modelled, and is not accounted for in the one-dimensional velocity model used in predicting phase arrival times. This effect is rarely a significant problem with shallow earthquakes, as the velocity structure along the depth-phase raypath for stations on difference sides of the focal sphere is little different, but at the extreme depth of this earthquake, depth phase bounce-points may be separated by 10's of km at the surface, which, in the case of this earthquake, can mean the difference between a depth phases passing through the basement-cored Wind River mountains, or through the sedimentary Wind River basement, with different velocity structures, and different elevations.

Given the azimuthal variation seen in the precise arrival times of depth phases, with a single depth unable to fit exactly all arrival times (see Figures 3,4,5), an error bound on our best-fit source depth of $\pm$ 8 km is calculated based on assuming a depth optimising the fits to all depth phase observations (underpredicting the delays in some case, overpredicting in others, and assuming an uncertainty in our velocity model of 10%). This uncertainty interval is consistent with the width of the misfit minima in the regional waveform inversion (Figure 2), and its variaton with reasonable changes in the location and velocity structure.

3.5 Focal mechanism estimation using relative amplitude methods

In studies of small to moderate size earthquakes, the relative amplitude method (Pearce, 1977, 1980) is often used to find orientations of the double-couple source that are compatible with the observed polarities and amplitudes of the phases P, pP and sP. In the relative amplitude method, as a result of microseismic noise and the interference of other phases arriving at similar times, there is some uncertainty in the amplitude of an observed phase. A nominal box-car probability function is used to define upper and lower amplitude bounds within which the true amplitude of each observed phase is judged to lie. As long as the focal mechanism is compatible with the observed polarities, and the computed relative amplitudes of P, pP and sP fall within the upper and lower relative amplitude bounds of the observed phases, the focal mechanism is deemed compatible.

We take eight vertical component seismograms from teleseismic stations with clear phase arrivals distributed around the focal sphere (discarding several where multiple observations from similar locations are available – e.g., Alaska). Table S2 gives the polarities and range of amplitudes assigned to direct P and the depth phase pP for the Wind River earthquake. The polarity of P could only be confidently determined from unfiltered seismograms for three of the eight stations. Amplitude observations are not included for MKAR as the IASPEI 1991 model predicts that the phase $pPcP$ will arrive at a similar time to pP, making the accurate measurement of the amplitude of pP difficult. We also do not include amplitudes for sP as this phase is very sensitive to the above-source structure and given the depth of the source and the uncertainty in the above-source wavespeeds and densities it is possible that acceptable focal mechanisms could be accidentally deemed incompatible.

Following the results of our regional tests for the importance of volumetric or deviatoric components of the moment tensor, we assume the Wind River earthquake is a double-couple source, and perform a grid search through orientation parameter space for solutions satisfying the relative amplitude bounds in Table S2 using increments of 5° for strike, dip and rake. We calculate the take-off angles of P and S using the wavespeed model in Table S1. As the data are relative amplitudes, the absolute scalar moment cannot be determined with this method.

Figure 6(a) is the vector plot (Pearce, 1977) displaying the range of compatible double-couple solutions. Vector plots display orientations of the double-couple (in the co-ordinate system of Pearce 1977, such that strike=σ[0°,360°], dip=δ[0°,180°], slip=ψ[0°,180°]) by plotting each compatible mechanism orientation as a unit vector drawn at an angle σ from the Cartesian point (ψ, δ). The existence of many focal mechanisms that are compatible with the observations supports our interpretation that the source is at a depth of approximately 75 km (in effect, supporting the correct identification of depth phases at times consistent with this depth). The teleseismic body wave observations do not however constrain the source orientation very well. Compatible focal mechanisms in the vector plot in Figure 6(a) include pure reverse faults, horizontal faults and dip-slip faults. The poor constraint is perhaps due to the low number of polarity observations, however normal faults are deemed incompatible due to the positive polarity observations at ILAR, PETK and MKAR.

3.6 Combined focal mechanism

To improve the constraint a set of observations places on the focal mechanism it is often preferable to use data observed at a range of distances and azimuths. For example, a detailed analysis of a small to moderate size earthquake in China (Selby et al., 2005) showed that while the teleseismic body wave data poorly constrains the strike of reverse faults, this can be resolved if surface wave data are included in the analysis. Many studies have therefore estimated the source parameters of seismic sources by combining regional and teleseismic waveforms (e.g., Baker and Doser, 1988; Holt and Wallace, 1987; Heyburn and Fox, 2010).

Figure 6(a) showed that there are many focal mechanisms which are compatible with the observed polarities and amplitudes of the phases P and pP. The teleseismic body waves on their own do not therefore adequately constrain the focal mechanism. Figure 6(b) shows focal mechanisms on a lower hemisphere stereographic projection which have a misfit within 10% of the minimum misfit found in the regional inversion. Whilst the regionally-derived focal mechanism is better constrained than for the teleseismic body waves, ranges of 45° to 70° for the strike, 35° to 85° for the dip and -10° to 40° for the rake (co-ordinate system of Aki and Richards, 1980) mean there is still a reasonable degree of uncertainty. To better constrain the focal mechanism we search the full covariance matrices from our two independent mechanism grid searches for focal mechanisms which are compatible with the observed polarities and amplitudes of the phases P and pP and also have a misfit within 10% of the minimum misfit found in the regional inversion. Acceptable solutions are those which fit all observed polarities, and have relative amplitudes for teleseismic phases within the uncertainty bounds as specified in Table S2, and which have misfits in the regional inversion within 10% of the minimum misfit. The lower hemisphere stereographic projection in Figure 6(c) shows the focal mechanism orientations which meet these criteria – only nine parameter combinations, on our 5° parameter grid. The focal mechanism is now well constrained with ranges of 50° to 60° for the strike, 75° to 85° for the dip and 30° to 40° for the rake thus demonstrating the usefulness of combining the two datasets. Our preferred focal mechanism has $\theta = 55°, \delta = 75°$ and $\phi = 35°$ (Figure 6(d)) and is chosen as in the regional inversion it has the lowest misfit of the nine focal mechanisms also compatible with the teleseismic relative amplitudes and polarities, displayed in Figure 6(c).

In all cases, regions where large-amplitude pP depth phases are observed (Eastern US, Figure 3; South America and the Caribbean, Figure 4), these are predicted by the radiation pattern (see Figures 3, 4) from our combined mechanism, even for stations not used in the relative amplitude calculations, reinforcing that these phases have been correctly identified, and are not sP phases from a shallower source depth. The same match between observation and prediction is also qualitatively true for sP observations in Alaska and Asia, despite these not being included in the relative amplitude calculations. Regional waveform synthetics for this combined mechanism are shown in blue on Figure 2. Differences between the best regional-only focal mechanism, and the waveforms for the combined mechanism at the teleseismically-constrained soruce depth are only significant on the vertical components of DUG and RLMT, where the combined mechanism underpredicts the amplitude of the Rayleigh wave, although we note that the signal-to-noise ratio at both stations is poor, and both stations are located close to nodal planes.

3.7 Waveform synthetics

To evaluate our best-fit focal mechanism, synthetic teleseismic P wave seismograms are calculated for our preferred focal mechanism at our best-fit overall source depth of 75 km. The short-period teleseismic P wave seismograms are calculated using the method of Douglas et al. (1972), and the finite source model of Savage (1966). Figure 7 shows the observed and synthetic short-period vertical component P waveforms calculated using the combined model source parameters and the source region structure in Table S1. As pP and particularly sP are particularly sensitive to the above-source structure, to improve the fit of the synthetic seismograms to the observed data, the thickness and wavespeed of the top sediment layer is modified slightly from the original model of Herrmann et al. (2011).

To match the scalar moment obtained from the regional inversion, a circular fault (Savage, 1966, model) with a radius of 0.85 km and a stress drop of 100 bars is used. Amplitude losses due to anelastic attenuation in the mantle are made using values of t^* between 0.38 and 0.75. These values (detailed on Figure 7) have been chosen so that the amplitude of the teleseismic synthetic waveforms generated using our combined source model match the observed amplitudes of teleseismic P-waves. However, we note that using a different set of elastic parameters in our regional inversion (which constrains the scalar moment) would result in a different moment, and require different t^* values.

The fit of the synthetic seismograms to the observed is mostly good. At SMRT, LPAZ, PTGA, and ESDC, the low amplitude P and large pP are modelled well. The large amplitude sPs at ILAR and USRK are also modelled well. At PETK where a simple seismogram is observed with no clear pP or sP, again the synthetic seismogram is in good agreement. At MKAR amplitude measurements were not included in the relative amplitude analysis however there is reasonable agreement between the observed and synthetic seismograms with P being the dominant phase on both seismograms. On the observed seismograms at MKAR two low amplitude arrivals are observed 21 sec and 33 sec after P. This is later than the arrivals interpreted as pP and sP at many of the other teleseismic stations which arrive at 18 sec and 28 sec. However as discussed above, $pPcP$ and $sPcP$ are predicted to arrive at a similar time to pP and sP so these two arrivals observed at MKAR may not in fact be pP and sP. The method of Douglas et al. (1972) does not model PcP and its depth phases so they are not seen on the synthetic seismograms.

Synthetic waveform polarities at LPAZ and ESDC appear that they may be incorrect. The application of a bandpass filter distorts the waveform (Douglas, 1997), and polarities were not clearly identifiable on the unfiltered trace, hence polarities at these stations were not included the mechanism inversion. We note that ESDC lies close for the P-wave nodal plane, and hence polarity reversal would require only a small change in orientation. We also note the potential for distortion due to filtering to be different between the synthetic and observed, due to an inaccurate representation of the source duration and rupture history.

3.8 Analysis of the aftershock using Pinedale array data

Finally, we make use of the location of the short-period array (vertical component only) and single broadband station (three-component) at Pinedale, WY, located on the south side of the Wind River Range (see Figure 1.b), and in close proximity to the earthquake epicentre ($\sim$ 42 km). In particular, we use this array to examine the aftershock reported by the NEIC at 15:15:34 UTC, approximately two hours after the main Wind River earthquake, and with a similar catalogue location. Whilst the small magnitude of the aftershock (M_W 3) makes is unsuitable for the analyses conducted so far in this paper, the proximity of Pinedale to both earthquakes means that a clear signal was recorded for both events. Figure 8(a) shows the unfiltered three-component waveforms from the broadband seismometer at Pinedale, aligned by the P arrival, and clearly demonstrates that the delay time between P and S arrivals for the mainshock event (red waveforms) is virtually identical to that for the aftershock (blue waveforms). A similar figure using all the short-period data from the Pinedale array is included in supplementary material (Figure S4). Figure 8(b) then shows the relative inter-station delay times for arrivals between short-period instruments within the Pinedale array. Delay times were calculated using picks for the initial peak, rather than the onset as for both earthquakes the onsets are low amplitude and difficult to pick meaning that onset picks could potentially be affected by variable noise levels across the array. The sampling interval for these instruments is 0.05 seconds and all inter-channel delays are within one sample of being the same for both the mainshock and aftershock, indicating that the apparent vector slowness across the array is the same for both events. Given the similarities in the delay time between P and S arrivals (in effect, the event-station distance), and in the apparent vector slowness, it is highly likely that the two events occurred in close proximity to each other. Hence, we conclude that the aftershock likely had a similar depth to the mainshock, and was also located in the lithospheric mantle.

4 Discussion

The depth of this earthquake (75 $\pm$ 8 km) makes it the second deepest earthquake yet identified in a stable continental region (excluding the special case of the India-Asia collision zone). The depth of the Moho in this areas is well constrained from combined surface-wave dispersion and receiver function studies, with local crustal thicknesss between 42 and 50 km (Shen et al., 2013). Hence, this earthquake occurred well within the mantle, and likely over 20 km deeper than the base of the crust. We are aware of only two other comparable earthquakes, occurring at significant depths into the continental mantle lithosphere: the 1979 Randolphe, Utah, earthquake at 90 km (Zandt and Richins, 1979), $\gtrsim$ 40 km into the mantle, and the 2000 Arafura Sea earthquake, at 61 ± 4 km, ~ 25 km into the mantle (Sloan and Jackson, 2012).

The extreme depth of this earthquake poses some interesting questions as to how it fits within our understanding of the rheology of the continental mantle, although the isolated nature of this earthquake makes it hard to draw any firm conclusions as to the underlying causative process. One possibility is that this earthquake may result from the migration of fluids within the mantle.

Microseismic activity in a variety of volcanic regions have been reported at depths significantly greater than would ordinarily be expected for seismogenesis – a phenomena typically ascribed to the high strain rates present during the movement of magma allowing the seismogenic, brittle failure of rocks at temperature where they normally deform in a ductile manner at lower tectonic strain rates (e.g. Keir et al., 2009; Reyners et al., 2007; Lindenfeld and Rümpker, 2011). The Wind River range is not an area of active surface volcanism, and the earthquake considered here is some 200 km from the current location of the Yellowstone hotspot, and its associated volcanism, in northwestern Wyoming (see Figure 1). There is little evidence for any connectivity between the magmatically active areas around Yellowstone, and our earthquake, with no intervening seismicity or volcanism, and a significant change in the seismic velocities between the source region of our earthquake, and the region underlying Yellowstone (Schmandt and Humphries, 2010). In addition, such magma-related seismicity is typically of limited maximum magnitude. Simple scaling relationships suggest that the Wind River earthquake ruptured an area of $\approx 10^6$ m^2. Whilst the relations governing such calculations are not strictly appropriate for magma-assisted earthquakes, the scale of the rupture patch is inconsistent with a magmatically-driven source process. The relatively large magnitude, the predominantly double-couple source, and the lack of any progressive sequence of seismicity, all argue in favour of a tectonic, rather than a magmatic or fluid-related origin. However, we cannot completely rule out the possibility that this isolated earthquake is the result of the migration of some form of fluid, potentially either as a distal effect of the Yellowstone plume, or as a result of the background migration of small-fraction melts within the mantle lithosphere.

The other main alternative, that this earthquake represents the brittle failure of the mantle as a result from tectonically-derived stresses, is similarly difficult to reconcile with our current understanding of continental seismogenesis. The prevailing view, drawn principally from the strong age-dependence of the thermal structure and seismogenic thickness of oceanic lithosphere (Wiens and Stein, 1983; Craig et al., 2014), is that seismicity in the oceanic mantle persists to depths consistent with $\approx 600°C$. The continental mantle earthquake under the epicratonic Arafura Sea was determined to lie near the boundary of a seismically-fast, cold region of lithosphere, with a probable temperature in the source region of close to, but less than, 600°C (Sloan and Jackson, 2012). However, the location and depth of the Randolphe, Utah, earthquake are unlikely to be so cold, if a 1-dimensional, steady-state thermal structure is assumed (Wong and Chapman, 1990). For the area of the Wind River earthquake, the interaction of the Yellowstone plume with the edge of cratonic North America, and uncertainties about the precise location of this edge, makes the thermal structure of the lithosphere here, along the margins of stable North America, hard to assess in detail. However, we do note that the source region lies marginally within the faster wavespeed region of the North American mantle which underlies much of stable North America (e.g. Schmandt and Humphries, 2010; Sigloch, 2011; Schmandt and Lin, 2014), often interpreted to represent cold, strong lithosphere, and within an area with relatively low surface heatflow (Mareschal and Jaupart, 2013). In addition, the mechanism orientation is consistent with an approximately N-S principle compressive stress direction, as demonstrated by the shallow regional seismicity in this area (Herrmann et al., 2011), suggesting it may be a response to the regionally coherent stress field. If indeed this earthquake is the result of brittle failure of the lithospheric mantle at close to 80 km depths, and hence is indicative of persistent lithospheric strength in this region to such depths, it poses some interesting geodynamic questions in terms of the forces required during the Laramide Orogeny to deform the Archean lithosphere in forming features such as the Wind River range. It would also suggest the potential for stable and extremely strong regions of the continental interior to experience extremely infrequent seismicity, presumably as a result of the long-term support of applied tectonic stresses.

Several hypothesis have been suggested to explain the occurrence of intermediate and deep-focus earthquakes within subducting lithosphere at depths and temperature believed to be inconsistent with normal brittle failure (e.g., transformational faulting, dehydration embrittlement, shear-heating). However, we consider these mechanisms are unlikely to apply to the case of the Wind River earthquake, given its location within a region of ancient, apparently stable, steady-state lithosphere.

5 Conclusion

We present a robust set of seismological analyses, taking advantage from a high-quality, globally distributed, dataset, demonstrating that the M_W 4.7 2013 Wind River earthquake occurred at a depth of 75 $\pm$ 8 km, with strike=55°, dip=75°, rake=35°. The depth of this earthquake places it some 20-30 km below the Moho in this region, well within the continental lithospheric mantle of North America. The interpretation of this in the context of the rheology of the continental mantle remains open to debate, due to the uncertain thermal structure along the craton boundary in this region, and the potential distal influence of the Yellowstone plume.

Acknowledgements

The data used in this study were retrieved through the Incorporated Research Institutions for Seismology Data Management Center (IRIS DMC), and through the International Monitoring System (IMS). We are grateful to the editor, Peter Shearer, to Sean Ford, and to one anonymous reviewer for their comments on this manuscript. We also thank R.A. Sloan, K. Priestley and S. Roecker for useful discussions. TJC was funded by a postdoctoral fellowship from ENS Paris. We are also grateful to the Saint Louis University Earthquake Center for the availability of the Computer Programs in Seismology software package.

References

K. Aki and P. G. Richards. *Quantitative Seismology*. Freeman, New York, 1980.

M. R. Baker and D. I. Doser. Joint inversion of regional and teleseismic earthquake waveforms. *Journal of Geophysical Research*, 93:2037–2045, 1988.

R. R. Blandford. An automatic event detector at the Tonto Forest Seismic Observatory. *Geophysics*, 39:633–643, 1974.

E. Burov. The equivalent elastic thickness (T_e), seismicity and the long-term rheology of continental lithosphere: Time to burn-out 'crème brûlée'? Insights from large-scale geodynamic modeling. *Tectonophysics*, 484:4–26, 2010.

W.-P. Chen and P. Molnar. Focal depths of intracontinental and intraplate earthquakes and their implications for the thermal and mechanical properties of the lithosphere. *Journal of Geophysical Research*, 88:4183–4214, 1983.

W.-P. Chen and Z. Yang. Earthquakes Beneath the Himalayas and Tibet: Evidence for Strong Lithospheric Mantle. *Science*, 304, 2004. doi: 10.1126/science.1097324.

T. J. Craig, A. Copley, and J. Jackson. Thermal and tectonic consequences of India underthrusting Tibet. *Earth and Planetary Science Letters*, 353-354: 231–239, 2012. doi: 10.1016/j.epsl.2012.07.010.

T. J. Craig, A. Copley, and J. Jackson. A reassessment of outer-rise seismicity and its implications for the mechanics of oceanic lithosphere. *Geophysical Journal International*, 197:63–89, 2014. doi: 10.1093/gji/ggu013.

A. Douglas. Bandpass filtering to reduce noise on seismograms: Is there a better way? *Bulletin of the Seismological Society of America*, 87:770–777, 1997.

A. Douglas, J. A. Hudson, and C. Blamey. A quantitative evaluation of seismic signals at teleseismic distances - III. Computed P and Rayleigh wave seismograms. *Geophysical Journal of the Royal Astronomical Society*, 28:385–410, 1972.

E. R. Engdahl, J. A. Jackson, S. C. Myers, E. A. Bergman, and K. Priestley. Relocation and assessment of seismicity in the Iran region. *Geophysical Journal International*, 167:761–778, 2006. doi: 10.1111/j.l365-246X.2006.03127.

E.R. Engdahl, R.D. van der Hilst, and R.P. Buland. Global teleseismic earthquake relocation with improved travel times and prceedures for depth determination. *Bulletin of the Seismological Society of America*, 88:722–743, 1998.

C. Frolich, W. Gan, and R. B. Herrmann. Two Deep Earthquakes in Wyoming. *Seismological Research Letters*, 86:810–818, 2015. doi: 10.1785/0220140197.

R. B. Herrmann. Computer Programs in Seismology: an evolving resource for instruction and research. *Seismological Research Letters*, 84:1081–1088, 2013. doi: 10.1785/0220110096.

R. B. Herrmann, H. Benz, and C. J. Ammon. Monitoring the Earthquake Source Process in North America. *Bulletin of the Seismological Society of America*, 101:2609–2625, 2011. doi: 10.1785/0120110095.

R. Heyburn and D. Bowers. Earthquake depth estimation using the F Trace and Associated Probability. *Bulletin of the Seismological Society of America*, 98:18–35, 2008. doi: 10.1785/0120070008.

R. Heyburn and B. Fox. Multi-objective analysis of body and suface waves from the Market Rase (UK) earthquake. *Geophysical Journal International*, 181:532–544, 2010. doi: 10.1111/j.1365-246X.2010.04523.x.

W. E. Holt and T. C. Wallace. A procedure for the joint inversion of regional and teleseismic long-period body waves. *Geophysical Research Letters*, 14: 903–906, 1987.

International Seismological Centre. *On-line bulletin*. Int. Seis. Cent., Thatcham, United Kingdom, 2012. http://www.isc.ac.uk.

J. Jackson, D. M^{c}Kenzie, K. Priestley, and B. Emmerson. New views on the structure and rheology of the lithosphere. *Journal of the Geological Society, London*, 165:453–465, 2008. doi: 10.1144/0016-76492007-109.

D. Keir, I. D. Bastow, K. A. Whaler, E. Daly, D. G. Cornwall, and S. Hautot. Lower crustal earthquakes near the Ethiopian rift induced by magmatic processes. *Geochemistry, Geophysics, Geosystems*, 10, 2009. doi: 10.1029/2009GC002382.

B. L. N. Kennett. IASPEI Seismological Tables. Research School of Earth Sciences, Australian National University, Canberra, 1991.

M. Lindenfeld and G. Rümpker. Detection of mantle earthquakes beneath the East African Rift. *Geophysical Journal International*, 186:1–5, 2011.

A. Maggi, J. A. Jackson, D. M^{c}Kenzie, and K. Priestley. Earthquake focal depths, effective elastic thickness, and the strength of the continental lithosphere. *Geology*, 28:495–498, 2000.

J.-C. Mareschal and C. Jaupart. Radiogenic heat production, thermal regime and evolution of continental heat crust. *Tectonophysics*, 609:524–534, 2013.

R. G. Pearce. Fault plane solutions using relative amplitudes of P and pP. *Geophysical Journal of the Royal Astronomical Society*, 50:459–487, 1977.

R. G. Pearce. Fault plane solutions using relative amplitudes of P and surface reflections: further studies. *Geophysical Journal of the Royal Astronomical Society*, 60:459–487, 1980.

R. W. Porritt, R. M. Allen, and F. F. Pollitz. Seismic imagin east of the Rocky Mountains with USArray. *Earth and Planetary Science Letters*, 402:16–25, 2014. doi: 10.1029/2010GC003421.

K. Priestley, J. Jackson, and D. McKenzie. Lithospheric structure and deep earthquakes beneath India, the Himalaya and southern Tibet. *Geophysical Journal International*, 172:345–362, 2008. doi: 10.1111/j.1365-246X.2007.03636.x.

M. Reyners, D. Eberhart-Phillips, and G. Stuart. The role of fluids in lower-crustal earthquakes near continental rifts. *Nature*, 446:1075–1078, 2007. doi: 10.1038/nature05743.

J. C. Savage. Radiation from a realistic model of faulting. *Bulletin of the Seismological Society of America*, 56:577–592, 1966.

B. Schmandt and F-C. Lin. P and S wave tomography of the mantle beneath the United States. *Geophysical Research Letters*, 41:6342–6349, 2014. doi: 10.1002/2014GL061231.

Brandon Schmandt and Eugene Humphries. Complex subduction and small-scale convection revealed by body-wave tomography of the western United States upper mantle. *Earth and Planetary Science Letters*, 297:435–445, 2010. doi: 10.1016/j.epsl.2010.06.047.

N. D. Selby, D. Bowers, A. Douglas, R. Heyburn, and D. Porter. Seismic discrimination in Southern Xinjiang: the 13 March 2003 Lop Nor earthquake. *Bulletin of the Seismological Society of America*, 95:No. 1, 197–211, 2005.

W. Shen, M. H. Ritzwoller, and V. Schulte-Pelkum. A 3-D model of the crust and uppermost mantle beneath the Central and Western US by joint inversion of receiver funciton and surface wave dispersion. *Journal of Geophysical Research*, 118:1–15, 2013. doi: 10.1029/2012JB009602.

K. Sigloch. Mantle provinces under North America from multifrequency P wave tomography. *Geochemistry, Geophysics, Geosystems*, 12, 2011. doi: 10.1029/2010GC003421.

R. A. Sloan and J. Jackson. Upper-mantle earthquakes beneath the Arafura Sea and south Aru Trough: Implications for continental rheology. *Journal of Geophysical Research*, 117, 2012. doi: 10.1029/2011JB008992.

C. M. Snelson, T. J. Henstock, G. R. Keller, and K. C. Miller. Crustal and uppermost mantle structure along the Deep Probe seismic profile. *Rocky Mountain Geology*, 33:181–198, 1998.

D. A. Wiens and S. Stein. Age dependence of oceanic intraplate seismicity and implications for lithospheric evolution. *Journal of Geophysical Research*, 88:6455–6468, 1983.

I. G. Wong and D. S. Chapman. Deep intraplate earthquakes in the western United States and their relationship to lithospheric temperatures. *Bulletin of the Seismological Society of America*, 80:589–599, 1990.

G. Zandt and W. D. Richins. An upper mantle earthquake beneath the middle Rocky mountains in NE Utah. *Earthquake Notes*, 50:69–70, 1979.

L. Zhu and D. V. Helmberger. Intermediate depth earthquakes beneath the India-Tibet collision zone. *Geophysical Research Letters*, 23:435–438, 1996.

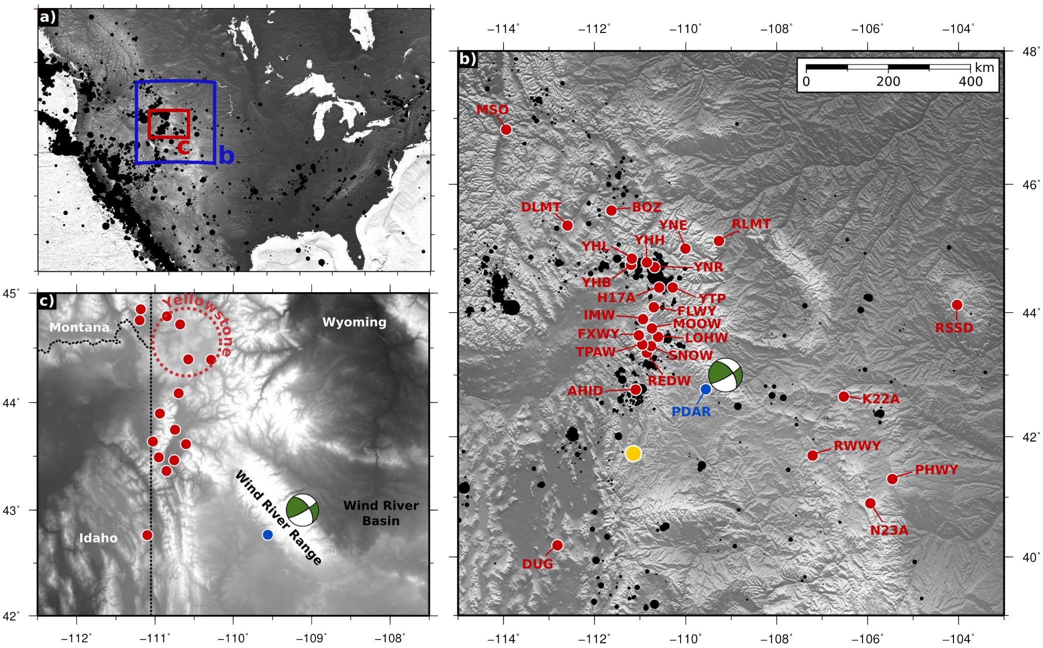

Figure 1: (a) Location map. Black points indicate seismicity from the NEIC catalogue, scaled by magnitude. (b) Regional context. Black points are again NEIC catalogue seismicity. Green mechanisms indicates the Wind River earthquake. Yellow circle indicates the 1979 Randolphe, Utah, earthquake at 90 km depth (Zandt and Richins, 1979). Red circles indicate the locations of regional seismic stations used in the regional waveform inversion (Figurse 2, S1, S2). Blue circle indicates the location of the Pinedale seismic array (PDAR) used in the aftershock analysis (Figures 8, S4. (c) Simple geological context, highlighting the location of the Wind River earthquake relative to the Wind River Range and Basin, and to the present location of the Yellowstone hotspot.

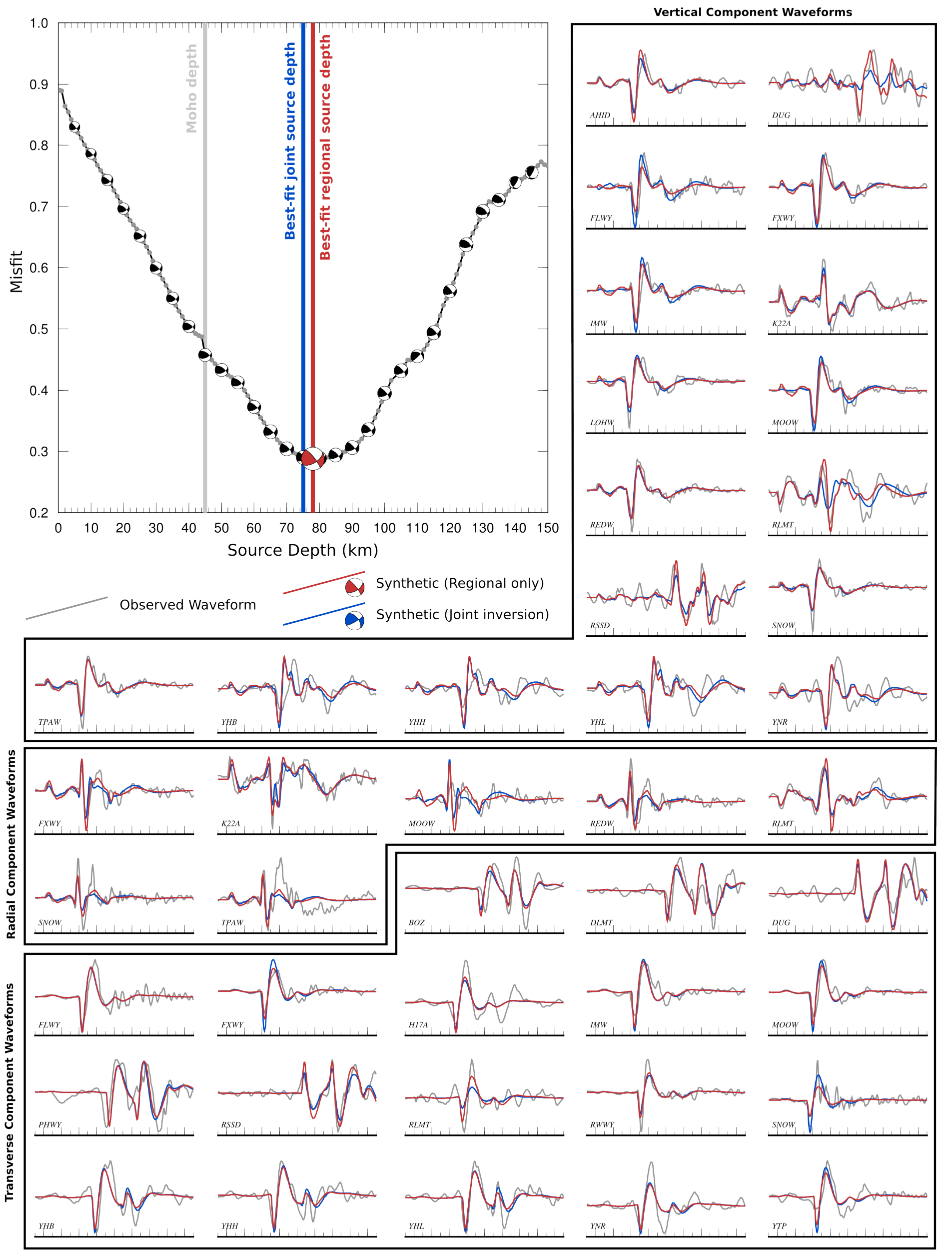

Figure 2: Results of the the regional waveform inversion. The panel in the top left shows how misfit evolves with varying depth. Best-fit focal mechanisms (aligned with 'north' along the misfit axis and 'east' along the depth axis) for a given depth are shown only at 5 km intervals, for clarity. The minimum misfit solution and depth are highlighted by the red focal mechanism and red bar. The remaining panels show the waveform fits for the overall minimum misfit solution. X-axis tick marks are 5 second intervals. Grey traces are observed data. Red traces are the aligned synthetic waveforms for the best-fit model. Blue traces are aligned synthetic waveforms for the mechanism determined by combination with the teleseismic relative amplitudes and polarities, at the depth consistent with the arrival times of depth phases. Waveforms are grouped into vertical, radial and transverse components, and are identifiable on Figure 1 by their station ID, shown on the bottom left of each seismogram.

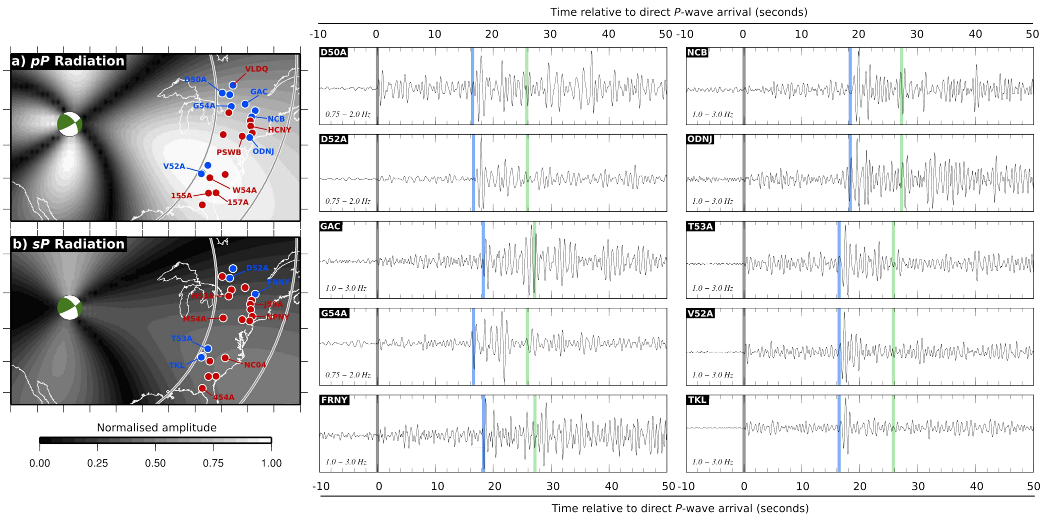

Figure 3: Analysis of broadband records at 20 – 30° epicentral distance. Panels (a) and (b) show the radiation patterns for pP and sP arrivals respectively, based on the focal mechanism determined from the joint regional and teleseismic amplitude inversion (shown by the green focal mechanism). Blue circles indicate the location of the stations corresponding to the remaining panels of the figure, identified by station ID. Red circles indicate those seismograms included on Figure S2. The remaining panels show broadband seismograms (bandpassed using a 4-pole Butterworth filter for the frequency range indicated). Grey, blue, and green bars indicate the predicted arrival times for P, pP, and sP phases respectively, calculated for a source depth of 75 km. If the station lies at an epicentral distance where triplications are predicted, the first-arrival triplication is taken for each phase.

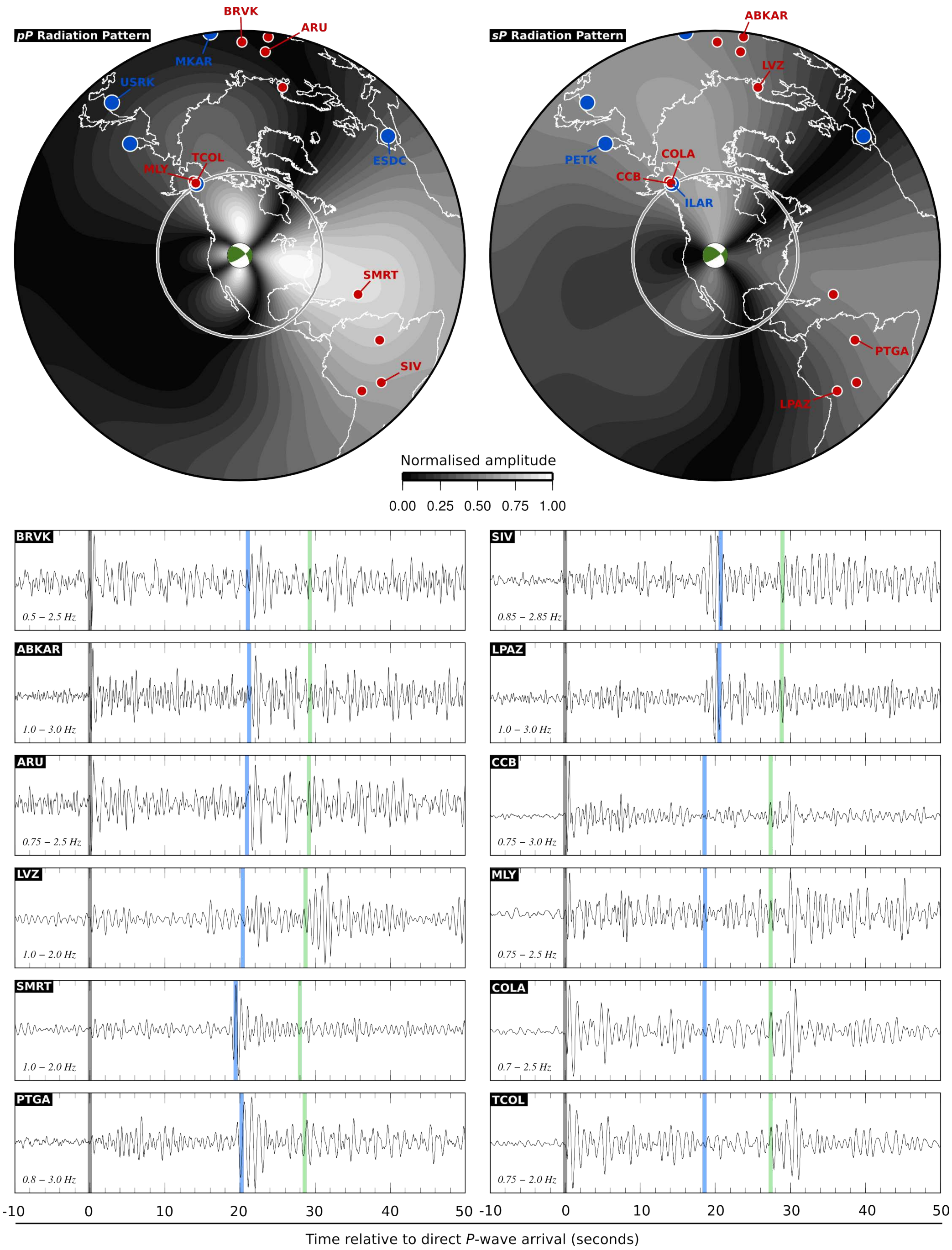

Figure 4: Broadband teleseismic records. The top two panels show the radiation patterns for pP and sP arrivals based on the focal mechanism determined from the joint regional and teleseismic amplitude inversion (shown by the green focal mechanism). Red circles show the location of single-station broadband seismometers shown on this figure. Blue circles show the location of multi-instrument arrays used in Figure 5. Lower panels shown broadband seismograms (bandpassed using a 4-pole Butterworth filter for the frequency range indicated). Grey, blue, and green bars indicate the predicted arrival times for P, pP, and sP phases respectively, calculated for a source depth of 75 km.

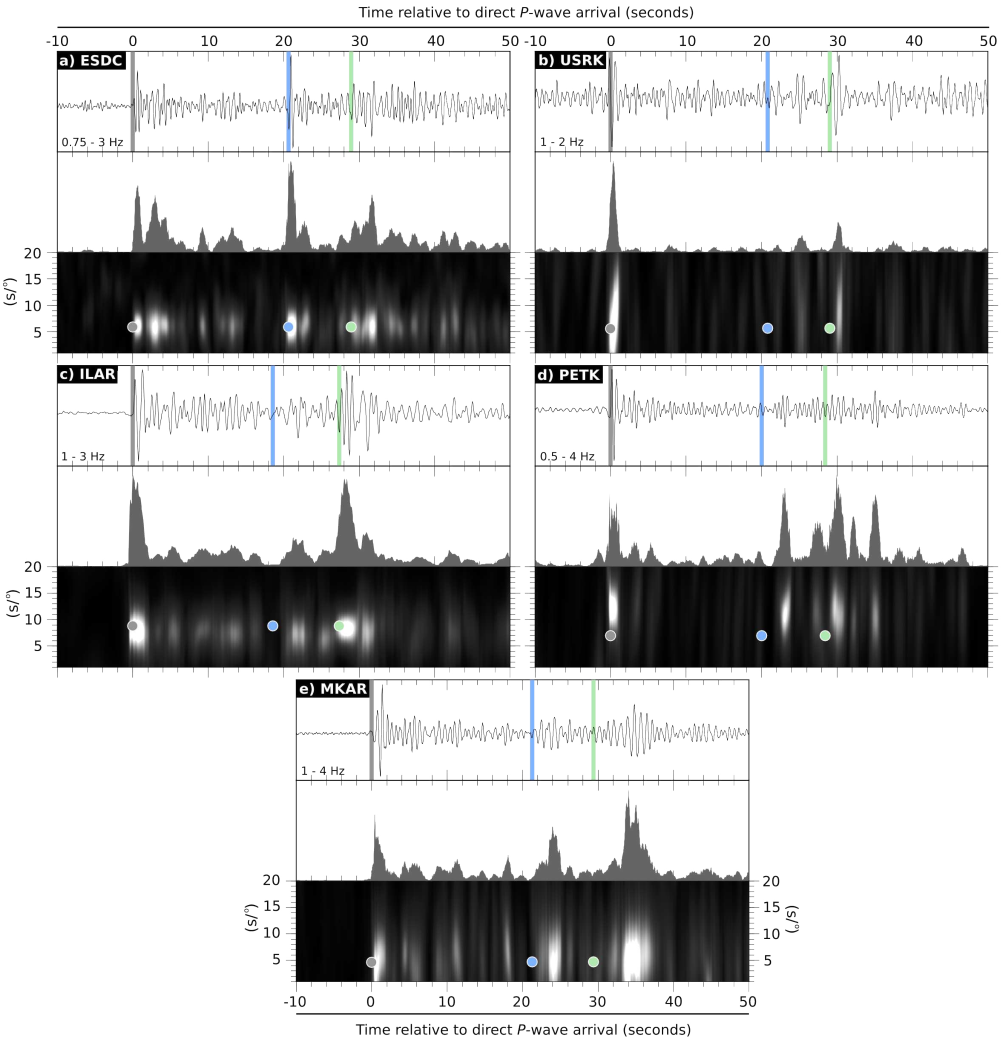

Figure 5: (a) – (e) Seismic array analysis at teleseismic distances. Array locations are identified by array ID on the radiation pattern plots on Figure 4. For each array, the top panel shows the bandpassed beamformed seismogram, for the pass band indicated, and at the azimuth and ray parameter predicted for the direct P wave arrival. Grey, blue, and green bars indicate the predicted arrival times for P, pP, and sP arrivals. The second panel shows the normalised F-statistic. The final panel shows a the F-statistic as a function of time and slowness. Grey, blue and green points show the predicted arrival times in time and slowness space for P, pP, and sP.

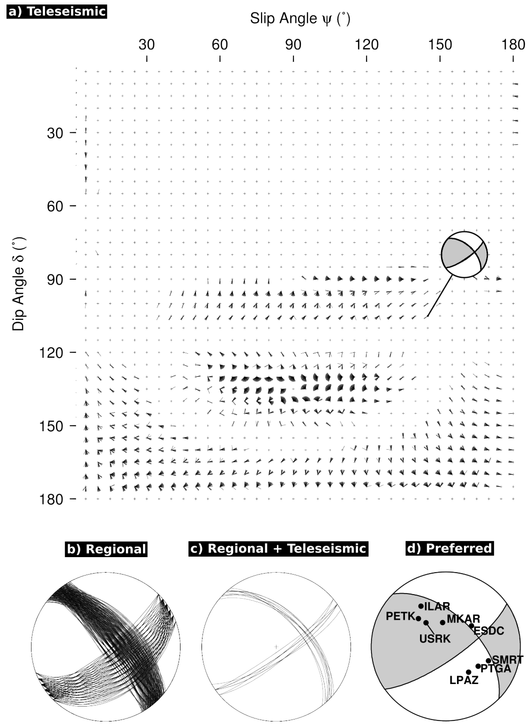

Figure 6: (a) Vector plot (Pearce, 1977) for the 21 September 2013 Wyoming earthquake showing the orientations of double-couples which are consistent with the observed polarities and amplitude bounds in Table S2. The lower-hemisphere stereographic projection shows the focal mechanism with the lowest calculated misfit in the regional inversion which is consistent with the observed polarities and amplitude bounds (shaded quadrants show compressional polarity). The coordinate system used is that of (Pearce, 1977). (b-d) Lower hemisphere stereographic projections showing: (b) Focal mechanisms which have a misfit within 10% of the minimum misfit in the regional inversion. (c) Focal mechanisms which have a misfit within 10% of the minimum misfit in the regional inversion and are compatible with the observed teleseismic body-wave polarities and amplitude bounds in Table S2. (d) Our preferred source orientation with stations used in the teleseismic body wave analysis marked on the projection. The positions of these stations are calculated using the take-off angles of P predicted by the IASPEI 1991 model (Kennett, 1991) for a source depth of 75 km.

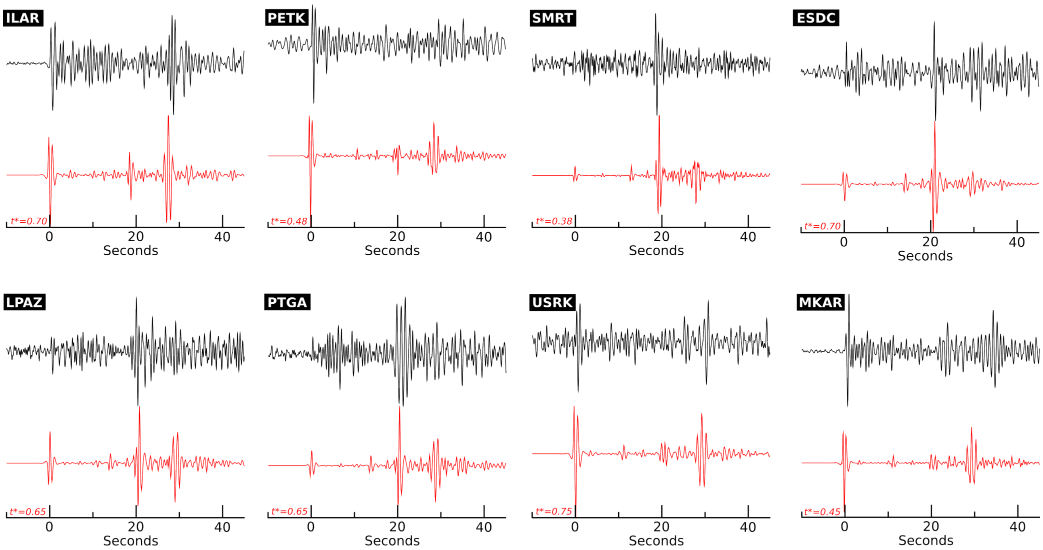

Figure 7: Observed (black) and synthetic (red) vertical component short-period waveforms calculated for our preferred source mechanism. The observed and synthetic seismograms have all been converted to a Yellowknife short-period response and have been filtered with a passband of 0.5-3.5 Hz. At each station the seismograms are plotted on a common amplitude scale. The values of $t*$ used in the calculation of each synthetic seismogram are reported on the lower left corner of each panel.

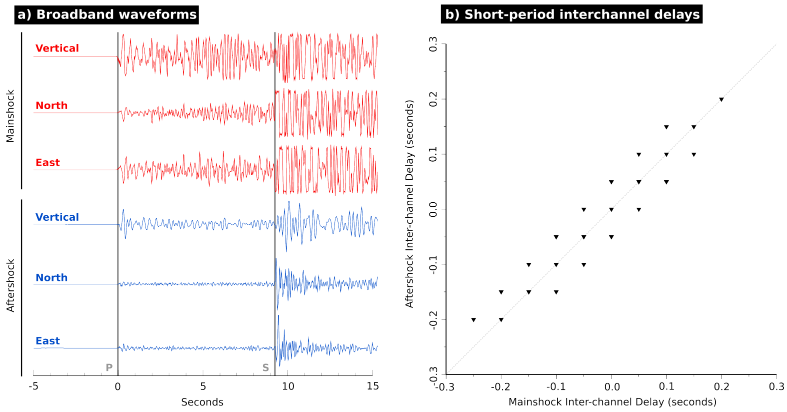

Figure 8: (a) Unfiltered broadband seismograms for the 3-component broadband seismometer at Pinedale for the main Wind River event (red) and the subsequent aftershock (blue). Traces are aligned on the P-wave arrival and amplitudes are normalised. Note that the S-wave arrival for the mainshock saturates the seismometer. (b) Relative delay times for P-wave arrivals at the short-period seismometers within the 13-instrument Pinedale array. Seismometer sampling rate is 0.05 seconds.